Effect of copper addition on cobalt-molybdenum electrodeposited coatings for the hydrogen evolution reaction in alkaline medium

Hugo Leandro Sousa Santos, Patricia Gon Corradini, Marina Medina, Lucia Helena Mascaro *

Department of Chemistry, Federal University of São Carlos, Rod. Washington Luiz, Km 235, CEP 13565-905, São Carlos-SP, Brazil

HIGHLIGHTS

- Co−Mo and Co−Mo−Cu coatings were obtained by a rapid electro-deposition process.
- Co−Mo−Cu materials promotes the hydrogen evolution by Volmer-Heyrovsky mechanism.
- $Co_{2.5}Mo_1Cu_1$ material presented a high stability.
- Copper addition favored the adsorption of intermediate species in the HER.

GRAPHICAL ABSTRACT

ARTICLE INFO
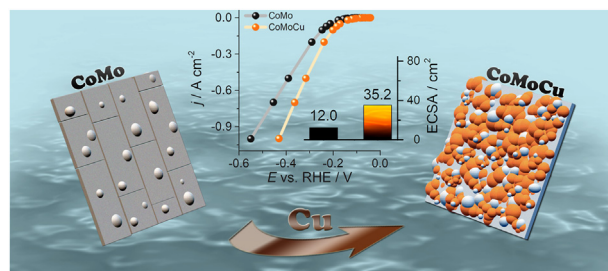
ABSTRACT

Co−Mo materials have been reported as electrocatalysts that present good performance in alkaline electrolytes. In this paper, the addition of copper into Co−Mo catalysts was evaluated for the hydrogen evolution reaction (HER). It was observed that the electrochemical activity of the Co−Mo for the HER benefited from the addition of copper. The overpotentials required to reach a current density of -10 mA cm^{-2} were of -156 mV and -119 mV for $Co_{67}Mo_{33}$ and $Co_{56}Mo_{21}Cu_{23}$, respectively. Besides the increased surface area resulting from the addition of copper, it was observed that the improved intrinsic activity for $Co_{61}Mo_{32}Cu_7$, compared to $Co_{67}Mo_{33}$, is related to a thermodynamic favoring of the hydrogen adsorption and desorption stages. Large quantities of copper do not favor the HER; therefore, the increased catalytic activity depends on a balance between the intrinsic catalytic activity and the increase of the electroactive area.

© 2020 Hydrogen Energy Publications LLC. Published by Elsevier Ltd. All rights reserved.

Introduction

The 21st century has been marked by concern about the environment. The scientific community generally recognizes that excessive consumption of fossil fuels not only leads to a decrease in reserves, but also negatively impacts the environment, affecting the global climate and resulting in health risks [1–3]. To minimize the use of non-renewable fossil fuels, there is an incentive to use hydrogen-fueled technologies [4]. Hydrogen gas is considered a sustainable fuel, since it can be produced by renewable sources using energy from the sun, tides, wind, and biomass [4–6], besides the electrolysis of water [7,8]. In this approach, electrolyzers for water splitting have been investigated in the literature, because the electrolysis enables the storage of energy in hydrogen bonds while reducing seasonality effects inherent of renewable sources [9]. Currently, obtaining hydrogen gas from electrolysis is expensive, mainly due to the application of noble-metal electrocatalysts [10].

Aiming to reduce costs, catalysts based on non-noble transition metals, such as metal sulfides [11–13], metal nitrides [14,15], metal selenides [16–18] and transition-metal alloys [19–21] have been widely studied and present very interesting results. Especially for electrocatalysts, the desired features are high current density at a small overpotential, high electronic conductivity, good charge transfer kinetics, and electrochemical stability for continuous H_2 production [10,22]. Metal alloys present all those characteristics, especially for the hydrogen evolution reaction (HER) in basic medium.

The HER is a heterogeneous catalytic process, in which the rate-determining step can be the adsorption of the proton on the catalyst surface. There must be an optimal hydrogen adsorption energy value, in the sense that the adsorption cannot be so strong as to hinder the hydrogen desorption, and neither so weak that an inefficient number of reactant protons are present; this behavior is well-described by Sabatier's principle. Alloy electrocatalysts present greater activity due to the electronic structure modification of the d-band center, which results in appropriate binding energy to stabilize the adsorbed hydrogen, favoring the formation of H_2 [10,23]. Analyzing the electronic configuration, Co can be understood as a hyper-d-metal and, when used as a cathode material, it presents some electrocatalytic activity for the HER. However, it was observed that combining this type of metal with hypo-d-metals, such as Mo, Ti, W, among other, results in interesting electrocatalytic characteristics, due to a significant synergistic effect [24]. The Co–Mo synergism has been demonstrated in different types of materials such as metallic alloys [25], phosphides [26], sulfides [27], and even in mixtures of compounds of different classes, such as $MoSe_2$/CoP and Mo_2C/Co, which can lead to superior catalytic activity [28,29]. But, Anantharaj and Noda commented that there is still room to further improve the catalytic activity of Co-based materials, even though they are widely studied [30]. Some reported Co-based materials still require high overpotentials to promote useful current densities and are unstable during prolonged operation [25].

In this study, the use of ternary Co–Mo–Cu for the HER in alkaline medium is reported, aiming to obtain a robust, stable, and low-cost catalyst. The catalysts were physically and electrochemically characterized using scanning electron microscopy (SEM), X-ray diffraction (XRD), X-ray photoelectron spectroscopy (XPS), polarization curves, and electrochemical impedance spectroscopy (EIS). The performance of the materials is also discussed based on the effect of the intrinsic catalytic activity, enriching the understanding of the HER mechanism.

Materials and methods

Preparation of the Co–Mo and Co–Mo–Cu coatings

Co–Mo and Co–Mo–Cu coatings were obtained by electrodeposition on carbon steel 1010 disk, with 0.196 cm^2 of geometric area. A typical three-electrode electrochemical cell was employed to deposit the material, with $Ag_{(s)}|AgCl_{(s)}|KCl_{(sat.)}$ as the reference electrode and a Pt grid, with area at least 2 times greater than the working electrode, as the counter electrode. Before the depositions, the working electrodes were polished using 600 grit sandpaper, followed by immersion in a KOH solution (30% w/v, 2 min) to degrease the surface.

The deposition solutions were prepared with a fixed Mo/Co molar ratio (0.2) and different molar ratios of Cu/Co were evaluated (0; 0.01; 0.05; 0.10). The precursors were: 0.1 mol L^{-1} cobalt sulfate hexahydrate ($CoSO_4.6H_2O$; Sigma 98%), 0.02 mol L^{-1} sodium molybdate (Na_2MoO_4, Synth 99%) and 0.001, 0.005, and 0.01 mol L^{-1} copper (II) sulfate pentahydrate ($CuSO_4.5H_2O$, Alfa Aesar 99%). Moreover, 0.2 mol L^{-1} sodium citrate ($Na_3C_6H_5O_7$, Synth 99%) was used as complexing agent and 0.5 mol L^{-1} sodium sulfate (Na_2SO_4, Synth 99%) was the supporting electrolyte, as recommended in the literature [19]. The pH of all baths was adjusted to 8 with NH_4OH. The Co–Mo and Co–Mo–Cu deposits were obtained galvanostatically at −30 mA cm^{-2} for 40 min, at room temperature (about 25 °C).

Physical characterization

The elemental mapping and compositions of Co–Mo and Co–Mo–Cu were estimated by energy-dispersive X-ray spectroscopy (EDX), using a FEI-XL30-FEG coupled to the detector Oxford Instruments-Link ISIS 300. Scanning electron microscopy (SEM) with high-resolution field emission, using a FEG-SEM ZEISS SUPRA 35, was employed to characterize the morphology of the electrodes.

The X-ray diffraction (XRD) analyses were performed using a diffractometer Rigaku - DMax2500PC (Cu Kα, 1.5406 Å, 40 kV). X-ray photoelectron spectroscopy (XPS) analyses were performed on a spectrometer Scienta Omicron, model ESCA 2SR. Mg Kα monochromator was used, calibrated using the C1s peak (284.8 eV).

Electrochemical characterization

The HER performance of the Co–Mo and Co–Mo–Cu coatings, were evaluated by stationary cathodic polarization curves, in KOH 6.0 mol L^{-1} at 25 °C. At each point, a current transient measurement (chronoamperometry) of 6 min was performed, and 22 points were collected, in the range of current densities

from -7.0×10^{-6} to -1.0 A cm^{-2}, without IR-drop correction. For these measurements, Hg/HgO/KOH 6 mol L^{-1} was used as the reference electrode and the values of the potential obtained were converted to the reversible hydrogen electrode (RHE) using the relation: $E_{(RHE)} = E_{(Hg/HgO)} + 0.928$, where 0.928 is the potential in the Hg/HgO scale corresponding to 0 V vs RHE. This value was found through the calibration of the Hg/HgO reference electrode in the H$_2$-saturated 6 mol L^{-1} KOH electrolyte at 25 °C [31,32]. The calibration curve is shown in Fig. S1, available in the Supporting Information (SI).

The electrochemical impedance spectroscopy (EIS) technique was employed to clarify the charge-transfer kinetics and mechanism for the HER. The EIS data were measured in 6.0 mol L^{-1} KOH, 25 °C, at 0.0 V, -0.1, and -0.2 V vs. RHE, using an amplitude of 10 mV and the frequency range of 1 kHz-0.01 Hz. The coating that presented the best HER performance was also evaluated by cathodic polarization curves from 0 V to -0.4 V vs RHE, with a scan rate of 0.5 mV s^{-1}, at the temperature range from 293 to 343 K. For all coatings, the double-layer capacitance (C$_{dl}$) was estimated using cyclic voltammetry (CV) at the scan rates of 25, 50, 75, and 100 mV s^{-1}. For all coatings, the capacitive current density ($\Delta j = |j_c - j_a|/2$) measured was plotted versus the scan rates and the linear slope value obtained was considered equivalent to C$_{dl}$ [33,34]. From this, the electrochemical active surface area (ECSA) was calculated using the relation: ECSA = C$_{dl}$/C$_S$, where the value of C$_S$ is known as 0.040 mF cm^{-2} [33,34]. The stability test was conducted in KOH 6.0 mol L^{-1} during 48 h, applying a constant current density of -135 mA cm^{-2}.

Results and discussion

Composition and morphology of the Co—Mo and Co—Mo—Cu coatings

Table 1 presents the estimated composition for Co—Mo and Co—Mo—Cu, confirming the expected deposition of each metal. The literature explained that a low concentration of Cu in electrolytes is sufficient for the deposition of this metal, because Cu deposition takes place at the limiting current [35]. It was observed that the increase in the concentration of copper in the deposition bath raised the relative percentage of this metal linearly, from 5.7 to 32.4 at%. In contrast, the relative atomic concentration of Co, Mo, and O decreased in the films. The small quantity of oxygen observed in the coatings is related to the presence of oxides. The electrodeposition method commonly leads to obtaining mixed structures of metal and oxide [36]. To identify the samples, the atomic proportions to the composition detected in the EDX were

adopted, hence, the samples were named according to their atomic ratio as shown in Table 1.

The SEM images of the Co—Mo—Cu deposits can be seen in Fig. 1a–d. The surface of Co$_{67}$Mo$_{33}$ (Fig. 1a) presents spherical nodules, a typical morphology from Co—Mo deposition [37–39], which is observed even on nanorod templates. It is an interesting feature because it results in a larger surface area, compared to Ni—Mo and other materials [40]. Some cracks are also observed on the surfaces of Co$_{67}$Mo$_{33}$ (Fig. 1a) and Co$_{61}$Mo$_{32}$Cu$_7$ (Fig. 1b). Casciano et al. showed that the crack can go through the entire film and expose the substrate [37]. This characteristic indicates the existence of a high stress during the electrodeposition [39,41,42], which may be related to a deformation induced by Mo on the Co crystal lattice, because of the larger atomic radius of Mo [37]. Films prepared from the bath solution with 20–40 at% Mo present cracks when produced by the electrodeposition method at a current density applied in the range of 10–100 mA cm^{-2} [38]. However, by increasing the copper content, there is a morphological modification, without cracks and with the formation of cauliflower-like structures (Fig. 1c and d). Probably, the co-deposition of Cu reduces the residual stress on the cobalt crystal lattice and, in this way, it inhibits the formation of cracks. The presence of copper also modifies the surface area, which may affect the electroactivity of the film through a possible increase in the density of active sites for the HER. Fig. 1e presents the EDX elemental mapping for the Co$_{56}$Mo$_{21}$Cu$_{23}$ coating and it is observed that the cobalt, molybdenum and copper elements do not present preferential deposition spots on the cauliflower-shaped morphology, being homogeneously distributed on the substrate.

Fig. 2a shows the XRD profiles for all Co—Mo—Cu coating compositions. Few peaks are observed for Co$_{67}$Mo$_{33}$ and Co$_{61}$Mo$_{32}$Cu$_7$, suggesting that the films are amorphous structures. This behavior is common for films prepared through electrodeposition because in this process the metal atoms do not bond in a long-ordered range, which is necessary to obtain a crystalline structure [37]. Amorphous structures are beneficial for electrocatalysis since the volume and surface available for the reaction are increased in comparison to the same material in the crystalline form [30]. The peak close to 45° is attributed to fcc (111) cobalt. For Co$_{67}$Mo$_{33}$, it is possible to observe some spikes near 31.7°, 37°, 55°, and 65.6°, which matched to cubic Co$_3$O$_4$ (JCPDS card file No. 80–1545) [43]. For the trimetallic compositions, the Co$_3$O$_4$ peaks are not observed, but this does not rule out the presence of this species, since it may be present at low concentration or as an amorphous structure. Cu—Mo alloy peaks were not observed, and this is expected because the Cu—Mo system is

Table 1 – Chemical composition determined by the EDX technique for Co—Mo—Cu electrodeposited films.

Bath composition Co:Mo:Cu (at%)	Co (at%)	Mo (at%)	Cu (at%)	O (at%)	Atomic composition Co:Mo:Cu	Sample nomenclature
5:1:0	55.6 ± 0.2	27.4 ± 0.4	–	18.0 ± 0.5	67:33:0	Co$_{67}$Mo$_{33}$
5:1:0.01	50.1 ± 0.8	26.7 ± 0.6	5.7 ± 0.2	18 ± 1.4	61:32:7	Co$_{61}$Mo$_{32}$Cu$_7$
5:1:0.05	48.3 ± 0.3	18.6 ± 0.2	20.0 ± 0.4	13.1 ± 0.5	56:21:23	Co$_{56}$Mo$_{21}$Cu$_{23}$
5:1:0.1	40.0 ± 0.2	15.5 ± 0.4	32.4 ± 0.5	12.2 ± 0.7	46:18:37	Co$_{46}$Mo$_{18}$Cu$_{37}$
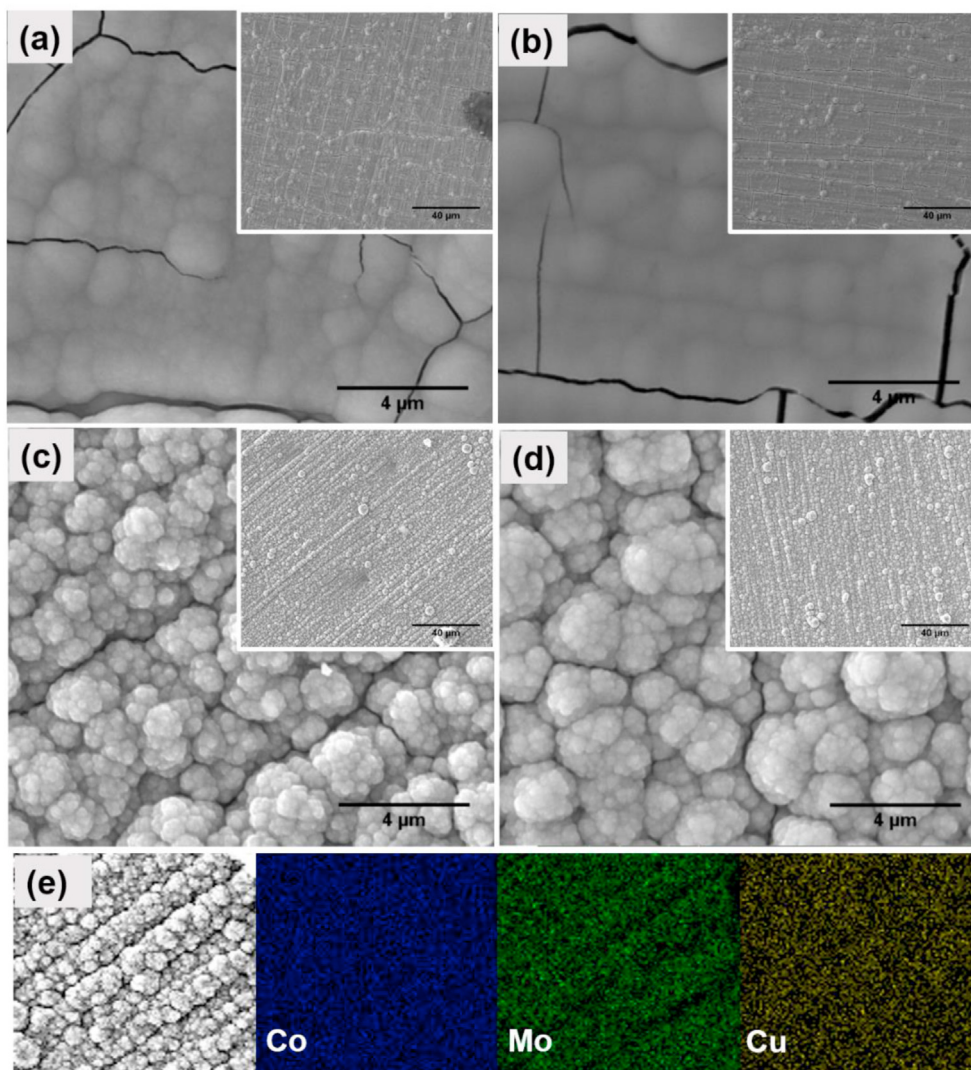
Fig. 1 — SEM images of (a) $Co_{67}Mo_{33}$, (b) $Co_{61}Mo_{32}Cu_7$, (c) $Co_{56}Mo_{21}Cu_{23}$ and (d) $Co_{46}Mo_{18}Cu_{37}$. (e) SEM image and corresponding EDX elemental mapping of $Co_{56}Mo_{21}Cu_{23}$, where Co (blue), Mo (green), and Cu (yellow) are identified. (For interpretation of the references to color in this figure legend, the reader is referred to the Web version of this article.)
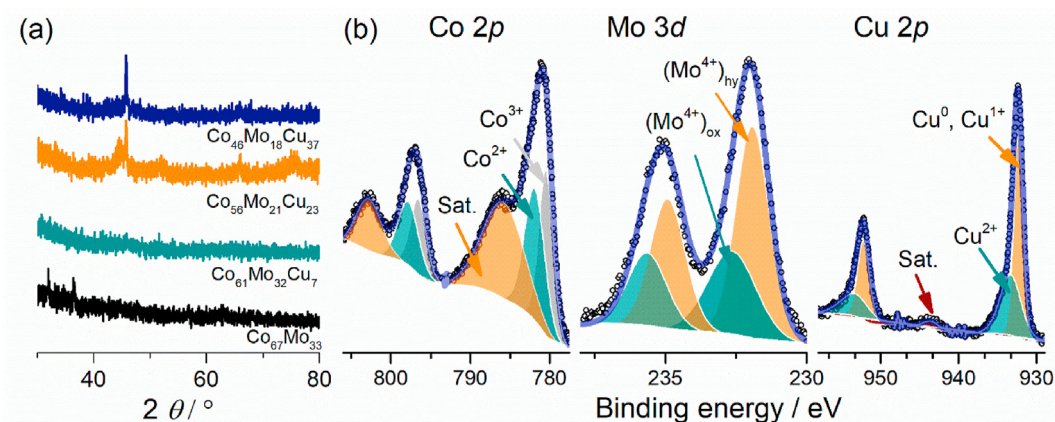

Fig. 2 — (a) XRD profiles of Co—Mo—Cu coatings. (b) Core-level XPS spectra of Co 2p, Mo 3d, and Cu 2p of $Co_{56}Mo_{21}Cu_{23}$ coating.

characterized by a positive enthalpy of mixing ($+18$ kJ mol^{-1}), and it is difficult to synthesize even by liquid-phase metallurgy [44].

Fig. 2b shows the core level XPS spectra of Co 2p, Mo 3d, and Cu 2p for the $Co_{56}Mo_{21}Cu_{23}$ coating. For Co 2p, the signal could be split into three duplets, located at Co 2$p_{3/2}$ with binding energy (BE) values of 780.4, 781.9, and 785.8 eV, which are in agreement with those reported for the Co^{3+}, Co^{2+} species, and a shake-up satellite peak, respectively [43,45,46]. The ratio of Co^{2+}/Co^{3+} is close to 1, indicating that there is no preferential oxidation state for Co on the surface. On the Mo 3$d_{5/2}$ profile, only the Mo^{4+} species was detected, on hydroxide and oxidized forms, at 231.8 eV and 232.7 eV, respectively [47]. The Cu 2$p_{3/2}$ region could be fitted into two duplets: 932.4 eV and 933.3 eV, which are related to reduced copper species (Cu^0 and Cu^{1+}) and Cu^{2+}, respectively [48–50]. The presence of a satellite peak at 943.5 eV confirms the presence of Cu (II) [51,52]. The superficial atomic composition estimated by the XPS measurements was 58:21:21 (Co:Mo:Cu), which is similar to the composition determined from EDX.

Electrochemical activity of the Co–Mo and Co–Mo–Cu coatings

The electrocatalytic performance of Co–Mo and Co–Mo–Cu coatings for the HER was investigated by stationary cathodic polarization, as shown in Fig. 3a. It can be observed that the $Co_{67}Mo_{33}$ coating had the lowest catalytic activity among the coatings produced, because this material required overpotentials of -156 and -247 mV, to reach current densities of -10 and -100 mA cm^{-2}, respectively. On the other hand, $Co_{56}Mo_{21}Cu_{23}$ presented the lowest overpotential values, requiring -119 and -200 mV to reach -10 and -100 mA cm^{-2}, respectively. Although less active than $Co_{56}Mo_{21}Cu_{23}$, the $Co_{61}Mo_{32}Cu_7$ and $Co_{46}Mo_{18}Cu_{37}$ coatings presented better performance than $Co_{67}Mo_{33}$, requiring -133 and -122 mV, respectively, to reach -10 mA cm^{-2}; moreover, $Co_{61}Mo_{32}Cu_7$ and $Co_{46}Mo_{18}Cu_{37}$ required -230 and -226 mV to provide -100 mA cm^{-2}, respectively. Especially for high current densities, such as -1.0 A cm^{-2}, the addition of copper promotes a reduction of 22% on the overpotential when comparing $Co_{56}Mo_{21}Cu_{23}$ to $Co_{67}Mo_{33}$. Table S1 (available in the SI) presents

some electrocatalytic parameters for recently reported activities of cobalt-based catalysts. The $Co_{67}Mo_{33}$ composition obtained in the present study presents an intermediate value of η_{10} (overpotential required to reach -10 mA cm^{-2}), which is greater than some other values listed for Co and Co–Mo materials. However, to the best of our knowledge, the addition of copper decreased the value of η_{100} (overpotential required to reach -100 mA cm^{-2}) to one of the smallest presented in the literature for this type of material. The low overpotential for $Co_{56}Mo_{21}Cu_{23}$ ranks this coating among the most active recently published Co-based catalyst for the HER in alkaline medium (Tables S1 and SI).

The kinetics and reaction mechanism of the HER can be obtained from Tafel plots. Fig. 3b presents the Tafel plots obtained from the stationary cathodic polarization for the Co–Mo and Co–Mo–Cu materials. It can be observed that all coatings exhibited a similar Tafel slope (b_c), with values ranging between 82 and 95 mV dec^{-1}. The b_c is equal to 82 mV dec^{-1} for the $Co_{56}Mo_{21}Cu_{23}$ film, demonstrating the lowest potential value needed to increase the current density by one order of magnitude. This result is in accordance with the fact that the $Co_{56}Mo_{21}Cu_{23}$ film showed the best performance for the HER among the prepared coatings. The Tafel slope can also be related to the mechanism involved in the formation of hydrogen [53], which can occur through two distinct pathways: Volmer–Tafel or Volmer–Heyrovsky mechanisms. In alkaline medium, the $H_2O_{(l)}$ discharge step (Volmer step, eq. (1)), which leads to the adsorption of hydrogen (H_{ad}) on active sites of the electrode (M), is common for both mechanisms. If this reaction is the rate-determining step (r.d.s), the Tafel slope of ~118 mV dec^{-1} is observed. On the other hand, the second step of the mechanism may be the combination of two H_{ad} (Tafel step, eq. (2)) or an electrochemical desorption of the H_{ad} involving a new $H_2O_{(l)}$ molecule (Heyrovsky step, eq. (3)), leading to the production of $H_{2(g)}$. If the Tafel or Heyrovsky step is the r.d.s, a Tafel slope value of ~30 or ~40 mV dec^{-1}, respectively, will be measured [54,55]. The Tafel slopes observed for all Co–Mo and Co–Mo–Cu samples allow us to state that the Volmer–Heyrovsky mechanism was favored, independently of the Cu content. However, the value of 82 mV dec^{-1} for the b_c of $Co_{56}Mo_{21}Cu_{23}$ does
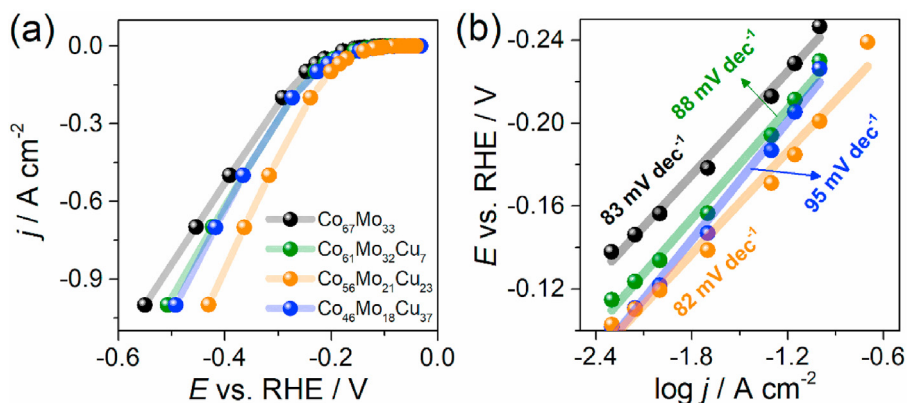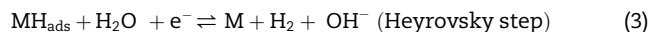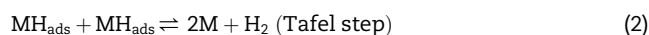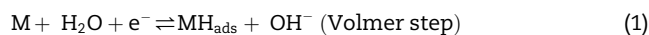

Fig. 3 – (a) Stationary linear polarization curves and (b) Tafel curves for the Co–Mo and Co–Mo–Cu films. Measured in KOH 6.0 mol L^{-1}, at 25 °C.

not allow one to state whether Volmer or Heyrovsky is the r.d.s, since the value is between 40 and 118 mV dec^{-1}.

$$M + H_2O + e^- \rightleftharpoons MH_{ads} + OH^- \text{ (Volmer step)} \quad (1)$$

$$MH_{ads} + MH_{ads} \rightleftharpoons 2M + H_2 \text{ (Tafel step)} \quad (2)$$

$$MH_{ads} + H_2O + e^- \rightleftharpoons M + H_2 + OH^- \text{ (Heyrovsky step)} \quad (3)$$

As an effort to elucidate the reaction mechanism of the HER for the electrode with the best catalytic activity (Co_{56}-$Mo_{21}Cu_{23}$), electrochemical impedance spectroscopy (EIS) measurements were performed at the potentials of 0.0 V, -0.1 V, -0.2 V $vs.$ RHE. The potentials were chosen in such a way that there was no evolution of hydrogen in profusion, since a significant release of bubbles from the surface of the electrode could interfere in the measurement.

From the Nyquist plots shown in Fig. 4a (and its insert) and the Bode diagrams (Fig. 4b), it is possible to observe that only one semicircle (one time constant) appears at 0 V vs RHE. In contrast, at -0.1 and -0.2 mV, the contribution of two semi-circles (two-time constants) can be observed. Based on these results, a 1T (model with one time constant) equivalent circuit was chosen to fit the impedance plots obtained at 0 V, while a 2 TP (model with two time constants in parallel) circuit was employed to describe the impedance plots obtained at -0.1 and -0.2 mV (Fig. 4c). These equivalent circuit models are used to relate the processes seen in the Nyquist and Bode plots to the physical processes that occur on the surface of the electrode and the electrode/electrolyte interface [56]. There-fore, R_s modeled the resistance of the solution, while the time

constant τ_1 (CPE–Rct), representing the semicircle at high frequencies, is attributed to charge transfer kinetics and related to the Heyrovsky step, with CPE corresponding to the double-layer capacitance and R_{ct} to the charge-transfer resistance. Furthermore, the time constant τ_2 (C_p–R_p), repre-senting the semicircle at low frequencies, is attributed to the adsorption of hydrogen on the active sites of the electrode and related to the Volmer step, with C_p corresponding to the pseudo-capacitance generated by the hydrogen adsorption and R_p to the resistance regarding the adsorption of hydrogen [32,56,57]. The EIS fitting parameters, for the $Co_{56}Mo_{21}Cu_{23}$, obtained for the 1T and 2TP equivalent circuits are presented in Table 2. Eq. (4), from Ref. [58], was used to calculate the equivalent capacitance (C_{dl}) from the CPE parameter.

$$C_{dl} = \left[\frac{CPE(T)}{\left(R_s^{-1} + R_{ct}^{-1}\right)^{(1-CPE(P))}} \right]^{1/CPE(P)} \quad (4)$$

At 0 V vs RHE (Table 2), the HER is not occurring yet, therefore, a high value of R_{ct} (25.4 Ω cm^2) is observed. In contrast, at the applied potentials of -100 and -200 mV, the R_{ct} values decrease dramatically to 3.20 and 0.53 Ω cm^2, respectively. On the other hand, the capacitance of the double layer (C_{dl}) increased slightly as more negative potentials were applied. The decrease of R_{ct} demonstrates an increase in the charge transfer rate, that is, the expected increase in the production of hydrogen with the increase in the applied overpotential. The slight increase in C_{dl} indicates that the in-crease in the rate of the HER, with consequent formation of bubbles, does not reduce the electroactive area of the elec-trode [57]. Analogously to R_{ct} and C_{dl}, the increase in the
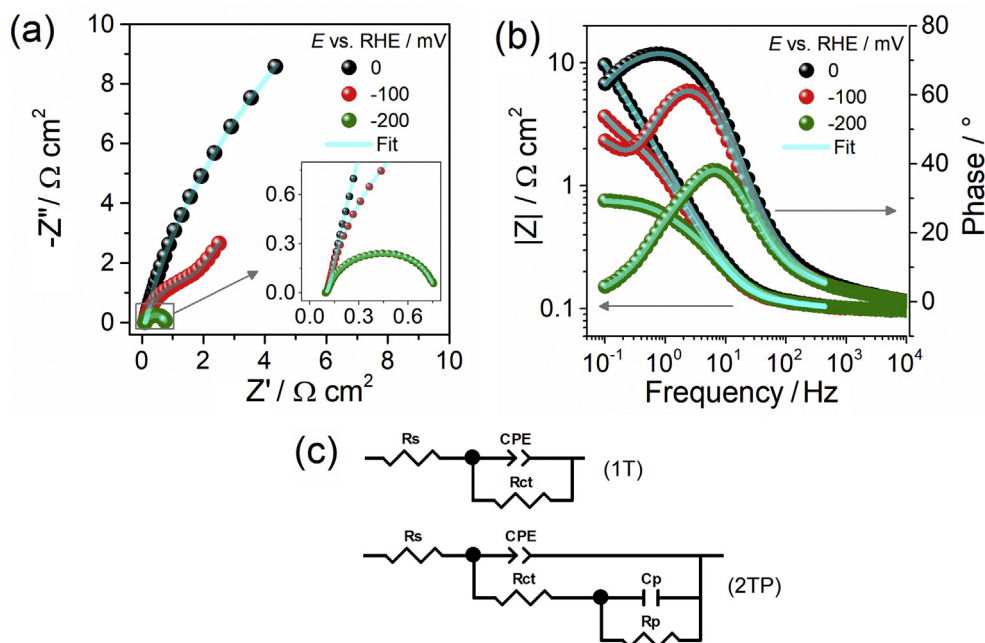

Fig. 4 — (a) Nyquist and (b) Bode plots for the $Co_{56}Mo_{21}Cu_{23}$ film at different applied potentials. (c) Equivalent circuit for fitting the EIS measurements. Experiments performed using KOH 6.0 mol L^{-1}, at 25 °C.

Table 2 – EIS fitting parameters for the $Co_{56}Mo_{21}Cu_{23}$ using the equivalent circuits shown in Fig. 4c (1T and 2TP) at 0, -100 and −200 mV vs RHE.

| E (mV vs RHE)	R_s (Ω cm^2)	R_{ct} (Ω cm^2)	R_p (Ω cm^2)	CPE (T)	CPE (P)	C_{dl} (mF cm^{-2})	C_p (mF cm^{-2})	χ^2
0	0.11	25.4	–	0.13	0.88	0.07	–	2.2×10^{-5}
−100	0.11	3.20	8.51	0.15	0.90	0.09	0.53	9.9×10^{-6}
−200	0.11	0.53	0.12	0.17	0.88	0.10	1.25	1.2×10^{-5}

applied potential led to a decrease in the R_p value (from 8.51 to 0.12 Ω cm^2) and an increase in the C_p value. This variation on the C_p/R_p parameters indicates that the discharge of water molecules for the adsorption of hydrogen is facilitated by the increased overpotential. Sa et al., ref. [54], employed CoN films as electrocatalysts for the HER and demonstrated that the Tafel slope of ~80 mV dec^{-1} indicates that both the Volmer and Heyrovsky steps are involved in the r.d.s, but one of the steps should be the slowest. Observing the higher value of R_{ct}, associated with Heyrovsky's step, concerning R_p, it is possible to state that Heyrovsky is the slower step.

A comparative study about the charge transfer kinetics for the Co−Mo and Co−Mo−Cu coatings was performed using EIS at the applied potential of −0.1 V vs RHE, the Nyquist plots are presented in Fig. 5a. For all coatings, two semicircles were observed in the Nyquist plots, therefore, a model equivalent circuit with two time constants in parallel (2TP), as shown in Fig. 4c, was used to fit the impedance spectrum. As mentioned above, the time constant at high frequencies, τ_1 (CPE−R_{ct}), is attributed to charge transfer kinetics. The fitting data are displayed in Table S2 (in the SI). The $Co_{56}Mo_{21}Cu_{23}$ coating exhibits the lowest charge transfer resistance (R_{ct}), of 3.20 Ω cm^2, when compared to $Co_{67}Mo_{33}$ (9.26 Ω cm^2), $Co_{61}Mo_{32}Cu_7$ (6.51 Ω cm^2), and $Co_{46}Mo_{18}Cu_{37}$ (6.46 Ω cm^2), indicating that $Co_{56}Mo_{21}Cu_{23}$ has the highest charge-transfer rate, therefore, a higher rate of evolution of hydrogen compared to other coatings. These impedance values are in agreement with the tendency of the catalytic activities for Co−Mo and Co−Mo−Cu coatings observed by stationary polarization curves, as shown in Fig. 3a.

The effect of varying the electrolyte temperature was studied for the $Co_{56}Mo_{21}Cu_{23}$ coating by linear polarization curves in a 6.0 mol L^{-1} KOH electrolyte. A Luggin capillary

was used to avoid any shift of the reference electrode potentials due to the temperature variation. The curves for each evaluated temperature are presented in Fig. S2a (in the SI). It can be noted that the increase of 50 K in the temperature of the electrolyte led to a reduction of 100 mV in the overpotential required to reach −10 mA cm^{-2}. The study of the influence of the electrolyte temperature on the catalytic activity for the HER allows the determination of an important kinetic parameter, which is the apparent activation energy (ΔE_{at}). The ΔE_{at} was estimated for the $Co_{56}Mo_{21}Cu_{23}$ catalyst. For each polarization curve, at different temperatures, the Tafel curves were constructed (Fig. S2b, in the SI) and the exchange current density (j_0) was determined using the Tafel equation in the same way as in the study reported by Wu et al. [59]. The j_0 values are presented in Table S3 (also in the SI). The value of ΔE_{at} was determined plotting j_0 vs. T^{-1} (Fig. 5b) and using the Arrhenius equation [60]. For $Co_{56}Mo_{21}Cu_{23}$, the ΔE_{at} is of 17 kJ mol^{-1}. This value is lower than observed for other Co-based catalysts, such as CoN/C (25 kJ mol^{-1}), CoW (28 kJ mol^{-1}), and Ni-based catalysts, such as NiMo (22 kJ mol^{-1}) and NiMoCu alloys (21 kJ mol^{-1}), which are among the most applied materials for HER [32,54,61]. The lower activation energy of $Co_{56}Mo_{21}Cu_{23}$ for HER compared to other aforementioned values from the literature reinforces the superior intrinsic activity of this material.

Stability is a crucial feature for an efficient HER catalyst. Therefore, the stability of $Co_{56}Mo_{21}Cu_{23}$ was evaluated by continuous electrolysis measurements during 48 h, under a current density of −135 mA cm^{-2}, in a 6.0 mol L^{-1} KOH electrolyte. The result is shown in Fig. 6a. Curiously, $Co_{56}Mo_{21}Cu_{23}$ showed an improvement in the catalytic activity throughout the experiment. The potential necessary to deliver the applied
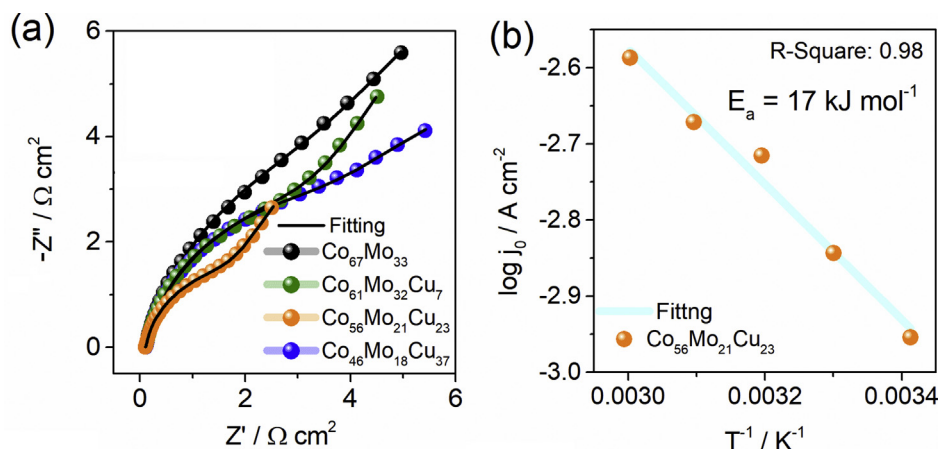
Fig. 5 – (a) Nyquist plots for Co−Mo and Co−Mo−Cu at −0.1 V vs RHE. (b) Arrhenius graph for the $Co_{56}Mo_{21}Cu_{23}$ coating.
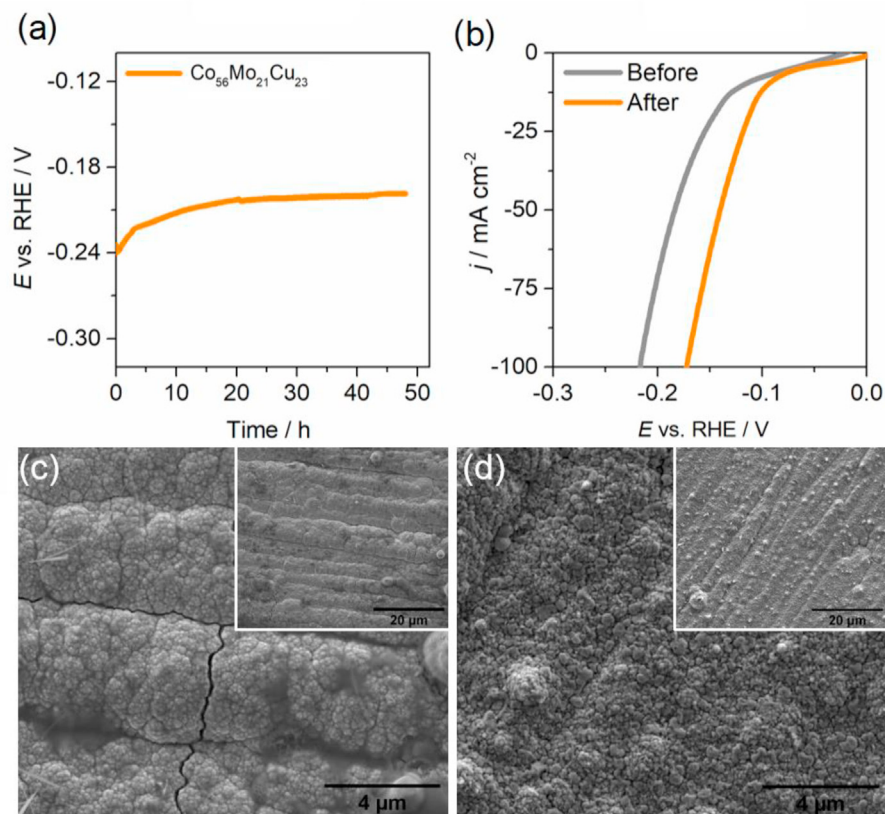
Fig. 6 – (a) Continuous water electrolysis (stability test) at -135 mA cm^{-2} for Co$_{56}$Mo$_{21}$Cu$_{23}$ catalyst and (b) Linear polarizations performed at 25 °C before and after the stability test in KOH 6.0 mol L^{-1} at 0.5 mV s^{-1}. Comparison of SEM surface images of Co$_{56}$Mo$_{21}$Cu$_{23}$ (c) before and (d) after the stability test.

current density decreased by 17.5% between the initial value (-240 mV) and the value at the end of the experiment (-198 mV). The gain in the activity is related to surface activation; similar processes have already been reported for cobalt-phosphide materials [62]. The electrochemical reduction of surface oxides and hydroxides is pointed out as the main reason for the activation. Since oxides and hydroxides are generally insulating and have low catalytic activity for the HER, they reduce the charge-transfer rate and the catalytic performance of the electrocatalyst [62–64]. Fig. 6b compares the polarization curves before and after the continuous electrolysis. It was observed that the Co$_{56}$Mo$_{21}$Cu$_{23}$ presented a better catalytic activity after 48 h of electrolysis. Before and after the stability test, the overpotentials of -117 mV and -95 mV, respectively, were required to deliver -10 mA cm^{-2}. SEM images of Co$_{56}$Mo$_{21}$Cu$_{23}$ before and after the stability test (Fig. 6c and d) were also obtained to evaluate the possible morphological changes resulting from the continuous evolution of hydrogen gas. There is no significant change in the surface morphology after the stability test. The slight morphological changes observed and the disappearance of cracks from the electrodeposition might have been due to a structural reorganization caused by the reduction of metal oxides. This did not affect the stability of the material, on the contrary, it improved its performance reducing the overpotential. As shown in Fig. 6b, the reduction of Co oxide was

the main factor that favored the activity of the catalyst, as observed in other papers [65–67].These results demonstrate that Co–Mo–Cu coatings, in addition to good catalytic activity, have excellent stability.

To clarify the better activity presented by Co–Mo–Cu coatings compared to Co–Mo, the capacitance of the double layer (C_{dl}) was determined by cyclic voltammetry (CV), the CVs are shown in Figs. S3a–d (in the SI). For this purpose, the CVs were performed in the capacitive regions of each coating at different scan rates. C_{dl} is equivalent to the slope of the straight line obtained by fitting the plot of the capacitive current density versus the scan rate (Fig. S3e, in the SI) [33,34]. The results showed an increase in the value of C_{dl} with the increase of the quantity of copper in the coatings, demonstrating an improvement in the surface roughness of the coatings [68]. From the C_{dl} values, the electrochemical active surface area (ECSA) was determined (see experimental part); they are shown in Fig. 7a. An extraordinary increase of the electroactive area is observed with the addition of copper. As an example, the Co$_{46}$Mo$_{18}$Cu$_{37}$ coating showed an ECSA value almost 12 times higher than the value for Co$_{67}$Mo$_{33}$. The large increase in the electroactive area is related to the increased surface roughness due to the morphological modifications by the addition of copper, as can be seen in the SEM images in Fig. 1. The fact that copper insertion has a significant effect on increasing the roughness of electrodeposited coatings has
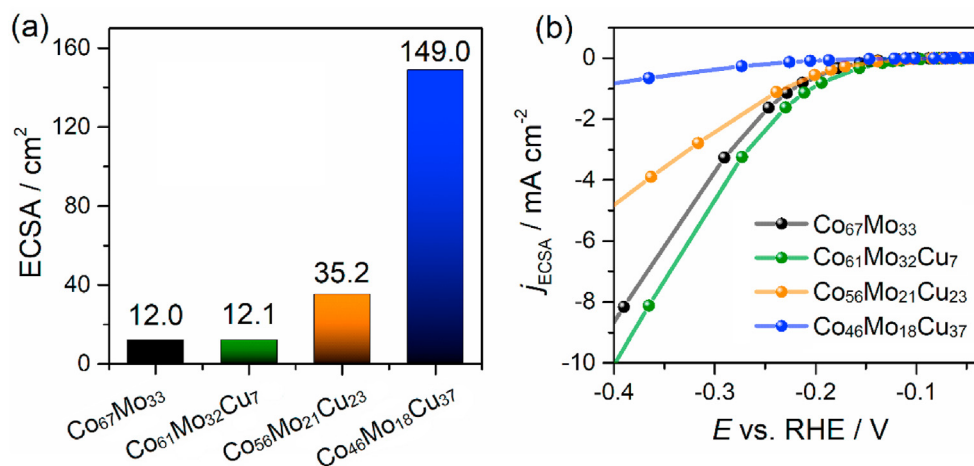
Fig. 7 − **(a) Electrochemical active surface area (ECSA) and (b) Stationary linear polarization normalized by the ECSA for the different coatings prepared.**

already been observed for other systems, such as Ni-Mo-Cu [19,32].

Although the increase of the surface area is of great importance, this is not the only factor that influences the catalytic activity of Co−Mo−Cu coatings, since $Co_{46}Mo_{18}Cu_{37}$ (149) has a much greater ECSA than $Co_{61}Mo_{32}Cu_7$ (12.1) and both samples present quite similar activities for the HER (Fig. 3a). Therefore, to evaluate the intrinsic catalytic activity of the samples without the interference of the surface area, the polarization curves of Fig. 3a were normalized by the ECSA (Fig. 7b). The increase in the quantity of copper in the films leads to a decrease in the intrinsic catalytic activity of the material, since the $Co_{56}Mo_{21}Cu_{23}$ and $Co_{46}Mo_{18}Cu_{37}$ films present 20% and 32% copper in their compositions, respectively. The decrease of the intrinsic catalytic activity can be attributed to a limited copper electroactivity [69]. Thus, the improvement of the copper-rich surface area does not necessarily reflect an increase, in the same proportion, of active sites for the HER. On the other hand, the $Co_{61}Mo_{32}Cu_7$ coating, which had only 5.7% of copper in its composition, presented the best intrinsic catalytic activity among the studied films. When evaluating nanotubular Cu-doped Ni films, Sun et al. demonstrated that 2% copper in the films led to a great improvement in the intrinsic activity of this material. The authors also demonstrated that Cu acts on the Gibbs free energy of hydrogen adsorption (ΔG_{H*}), leading to a value close to 0.0 eV, from which there is an optimal balance between the rate of proton reduction and the desorption of the hydrogen formed, related to a high activity for the HER [52]. Hence, the greater intrinsic activity for $Co_{61}Mo_{32}Cu_7$, compared to $Co_{67}Mo_{33}$, may be directly related to the thermodynamic favoring of the hydrogen adsorption and desorption stages, due to the presence of a specific quantity of copper. Overall, the best catalytic activity for the HER was observed for the $Co_{56}Mo_{21}Cu_{23}$ coating, because in this composition there is an ideal balance between the intrinsic catalytic activity and the gain of electroactive area, due to the presence of copper.

Conclusion

In summary, we have demonstrated that Co−Mo and Co−Mo−Cu alloys present a good electrocatalytic performance for the HER. It was observed that the electrochemical activity, regarding the HER, of the Co−Mo material improved by the addition of copper. The overpotentials required to obtain a current density of −10 mA cm^{-2} were of 156 mV and 119 mV for $Co_{67}Mo_{33}$ and $Co_{56}Mo_{21}Cu_{23}$, respectively.

Despite the increase of the surface area due to the addition of copper, it was observed that the better intrinsic activity of $Co_{61}Mo_{32}Cu_7$, compared to $Co_{67}Mo_{33}$, is related to a thermodynamic favoring of the hydrogen adsorption and desorption stages. To increase the catalytic activity, it is necessary to establish a balance between the intrinsic catalytic activity and the increase of the electroactive area, since large quantities of copper do not favor the HER.

Finally, the addition of copper in catalyst coatings that present smooth surfaces, such as Co−Mo, is a great way to increase the surface area of the material and the intrinsic catalytic activity. Thus, the application of this approach for other transition-metal catalysts will be investigated in future studies.

Declaration of competing interest

The authors declare that they have no known competing financial interests or personal relationships that could have appeared to influence the work reported in this paper.

Acknowledgements

Appendix A. Supplementary data

Supplementary data to this article can be found online at https://doi.org/10.1016/j.ijhydene.2020.09.128.

REFERENCES

[1] Panwar NL, Kaushik SC, Kothari S. Role of renewable energy sources in environmental protection. A review 2011;15:1513−24. https://doi.org/10.1016/j.rser.2010.11.037.

[2] Alaba PA, Abbas A, Daud WMW. Insight into catalytic reduction of CO_2: catalysis and reactor design. J Clean Prod 2017;140:1298−312. https://doi.org/10.1016/j.jclepro.2016.10.022.

[3] Spinner NS, Vega JA, Mustain WE. Recent progress in the electrochemical conversion and utilization of CO2. Catal Sci Technol 2012;2:19−28. https://doi.org/10.1039/C1CY00314C.

[4] Wang JY. Barriers of scaling-up fuel cells: cost, durability and reliability. Energy 2015;80:509−21. https://doi.org/10.1016/j.energy.2014.12.007.

[5] Gupta NM. Factors affecting the efficiency of a water splitting photocatalyst: a perspective. Renew Sustain Energy Rev 2017;71:585−601. https://doi.org/10.1016/j.rser.2016.12.086.

[6] Santos HLS, Corradini PG, Andrade MAS, Mascaro LH. CuO/NiOx thin film−based photocathodes for photoelectrochemical water splitting. J Solid State Electr 2020;24:1899−908. https://doi.org/10.1007/s10008-020-04513-5.

[7] Minggu LJ, Wan Daud WR, Kassim MB. An overview of photocells and photoreactors for photoelectrochemical water splitting. Int J Hydrogen Energ 2010;35:5233−44. https://doi.org/10.1016/j.ijhydene.2010.02.133.

[8] Guo Y, Tang J, Qian H, Wang Z, Yamauchi Y. One-pot synthesis of zeolitic imidazolate framework 67-derived hollow Co3S4@MoS2 heterostructures as efficient bifunctional catalysts. Chem Mater 2017;29:5566−73. https://doi.org/10.1021/acs.chemmater.7b00867.

[9] Walter MG, Warren EL, McKone JR, Boettcher SW, Mi QX, Santori EA, Lewis NS. Solar water splitting cells. Chem Rev 2010;110:6446−73. https://doi.org/10.1021/cr1002326.

[10] Patel PP, Hanumantha PJ, Datta MK, Velikokhatnyi OI, Hong D, Poston JA, Manivannan A, Kumta PN. Cobalt based nanostructured alloys: versatile high performance robust hydrogen evolution reaction electro-catalysts for electrolytic and photo-electrochemical water splitting. Int J Hydrogen Energ 2017;42:17049−62. https://doi.org/10.1016/j.ijhydene.2017.05.175.

[11] Medina M, Corradini PG, Mascaro LH. Facile one-step electrodeposition fabrication of amorphous MoS2 catalysts in titanium for hydrogen evolution reaction. J Braz Chem Soc 2019:1−9. https://doi.org/10.21577/0103-5053.20190115.

[12] Yang P, Wang B, Liu ZQ. Towards activation of amorphous MoSx via Cobalt doping for enhanced electrocatalytic hydrogen evolution reaction. Int J Hydrogen Energ 2018;43:23109−17. https://doi.org/10.1016/j.ijhydene.2018.10.215.

[13] Guo Y, Park T, Yi JW, Henzie J, Kim J, Wang Z, Jiang B, Bando Y, Sugahara Y, Tang J, Yamauchi Y. Nanoarchitectonics for transition-metal-sulfide-based electrocatalysts for water splitting. Adv Mater 2019;31:1807134. https://doi.org/10.1002/adma.201807134.

[14] Zhang W, Cui L, Liu J. Recent advances in cobalt-based electrocatalysts for hydrogen and oxygen evolution reactions. J Alloy Compd 2020;821:153542. https://doi.org/10.1016/j.jallcom.2019.153542.

[15] Zhang H, Chen X, Lin Z, Zhang L, Cao H, Yu L, et al. Hybrid niobium and titanium nitride nanotube arrays implanted with nanosized amorphous rhenium−nickel: an advanced catalyst electrode for hydrogen evolution reactions. Int J Hydrogen Energ 2020;45:6461−75. https://doi.org/10.1016/j.ijhydene.2019.12.173.

[16] Ding H, Xu G, Zhang L, Wei B, Hei J, Chen L. A highly effective bifunctional catalyst of cobalt selenide nanoparticles embedded nitrogen-doped bamboo-like carbon nanotubes toward hydrogen and oxygen evolution reactions based on metal-organic framework. J Colloid Interface Sci 2020;566:296−303. https://doi.org/10.1016/j.jcis.2020.01.096.

[17] Bhat KS, Nagaraja HS. Nickel selenide nanostructures as an electrocatalyst for hydrogen evolution reaction. Int J Hydrogen Energ 2018;43:19851−63. https://doi.org/10.1016/j.ijhydene.2018.09.018.

[18] Premnath K, Arunachalam P, Amer MS, Madhavan J, Al-Mayouf AM. Hydrothermally synthesized nickel molybdenum selenide composites as cost-effective and efficient trifunctional electrocatalysts for water splitting reactions. Int J Hydrogen Energ 2019;44:22796−805. https://doi.org/10.1016/j.ijhydene.2019.07.034.

[19] Xia M, Lei T, Lv NL, Li NF. Synthesis and electrocatalytic hydrogen evolution performance of Ni-Mo-Cu alloy coating electrode. Int J Hydrogen Energ 2014;39:4794−802. https://doi.org/10.1016/j.ijhydene.2014.01.091.

[20] Cabello G, Gromboni MF, Pereira EC, Mascaro LH, Marken F. Microwave-electrochemical deposition of a Fe-Co alloy with catalytic ability in hydrogen evolution. Electrochim Acta 2017;235:480−7. https://doi.org/10.1016/j.electacta.2017.03.117.

[21] Goranova D, Lefterova E, Rashkov R. Electrocatalytic activity of Ni-Mo-Cu and Ni-Co-Cu alloys for hydrogen evolution reaction in alkaline medium. Int J Hydrogen Energ 2017;42:28777−85. https://doi.org/10.1016/j.ijhydene.2017.10.002.

[22] Guo Y, Tang J, Wang Z, Kang Y-M, Bando Y, Yamauchi Y. Elaborately assembled core-shell structured metal sulfides as a bifunctional catalyst for highly efficient electrochemical overall water splitting. Nano Energy 2018;47:494−502. https://doi.org/10.1016/j.nanoen.2018.03.012.

[23] Wen S, Yang T, Zhao N, Ma L, Liu E. Ni-Co-Mo-O nanosheets decorated with NiCo nanoparticles as advanced electrocatalysts for highly efficient hydrogen evolution. Appl Catal B Environ 2019;258:117953. https://doi.org/10.1016/j.apcatb.2019.117953.

[24] Jaksic MM. Hypo−hyper-d-electronic interactive nature of interionic synergism in catalysis and electrocatalysis for hydrogen reactions. Int J Hydrogen Energ 2001;26:559−78. https://doi.org/10.1016/S0360-3199(00)00120-8.

[25] Laszczyńska A, Szczygieł I. Electrocatalytic activity for the hydrogen evolution of the electrodeposited Co−Ni−Mo, Co−Ni and Co−Mo alloy coatings. Int J Hydrogen Energ 2019;45:508−20. https://doi.org/10.1016/j.ijhydene.2019.10.181.

[26] Gong L, Lan K, Wang X, Huang X, Jiang P, Wang K, Yang M, Ma L, Li R. Carbon-coated Co-Mo-P nanosheets supported on carbon cloth as efficient electrocatalyst for Hydrogen Evolution Reaction. Int J Hydrogen Energ 2020;45:544−52. https://doi.org/10.1016/j.ijhydene.2019.10.248.

[27] Hou X, Li Y, Cheng L, Feng X, Zhang H, Han S. Cobalt-molybdenum disulfide supported on nitrogen-doped graphene towards an efficient hydrogen evolution reaction. Int J Hydrogen Energ 2019;44:11664−74. https://doi.org/10.1016/j.ijhydene.2019.03.159.

[28] Xia L, Zhang X, Song H, Zheng Y, Li X, Gao B, Huo K, Chu PK. Structural engineering of hierarchically heterostructured Mo2C/Co conformally embedded in carbon for efficient water splitting. Int J Hydrogen Energ 2020;45:22629−37. https://doi.org/10.1016/j.ijhydene.2020.06.049.

[29] Zhang L, Zhu J, Wang Z, Zhang W. 2D MoSe2/CoP intercalated nanosheets for efficient electrocatalytic hydrogen production. Int J Hydrogen Energ 2020;45:19246−56. https://doi.org/10.1016/j.ijhydene.2020.05.059.

[30] Anantharaj S, Noda S. Amorphous catalysts and electrochemical water splitting: an untold story of harmony. Small 2020;16. https://doi.org/10.1002/smll.201905779.

[31] Gao M-R, Liang J-X, Zheng Y-R, Xu Y-F, Jiang J, Gao Q, Li J, Yu S-H. An efficient molybdenum disulfide/cobalt diselenide hybrid catalyst for electrochemical hydrogen generation. Nat Commun 2015;6:5982. https://doi.org/10.1038/ncomms6982.

[32] Santos HLS, Corradini PG, Medina M, Dias JA, Mascaro LH. NiMo−NiCu inexpensive composite with high activity for hydrogen evolution reaction. ACS Appl Mater Interfaces 2020;12:17492−501. https://doi.org/10.1021/acsami.0c00262.

[33] Li Y, Zhao C. Enhancing water oxidation catalysis on a synergistic phosphorylated NiFe hydroxide by adjusting catalyst wettability. ACS Catal 2017;7:2535−41. https://doi.org/10.1021/acscatal.6b03497.

[34] McCrory CCL, Jung S, Peters JC, Jaramillo TF. Benchmarking heterogeneous electrocatalysts for the oxygen evolution reaction. J Am Chem Soc 2013;135:16977−87. https://doi.org/10.1021/ja407115p.

[35] Landolt D. Fundamental aspects of alloy plating. Plat Surf Finish 2001;88:70−9.

[36] Vernickaite E, Tsyntsaru N, Sobczak K, Cesiulis H. Electrodeposited tungsten-rich Ni-W, Co-W and Fe-W cathodes for efficient hydrogen evolution in alkaline medium. Electrochim Acta 2019;318:597−606. https://doi.org/10.1016/j.electacta.2019.06.087.

[37] Casciano PNS, Benevides RL, Santana RAC, Correia AN, de Lima-Neto P. Factorial design in the electrodeposition of Co-Mo coatings and their evaluations for hydrogen evolution reaction. J Alloy Compd 2017;723:164−71. https://doi.org/10.1016/j.jallcom.2017.06.282.

[38] Kublanovsky VS, Yapontseva YS. Electrocatalytic properties of Co-Mo alloys electrodeposited from a citrate-pyrophosphate electrolyte. Electrocatalysis 2014;5:372−8. https://doi.org/10.1007/s12678-014-0197-y.

[39] Gómez E, Pellicer E, Vallés E. Developing plating baths for the production of cobalt−molybdenum films. Surf Coating Technol 2005;197:238−46. https://doi.org/10.1016/j.surfcoat.2004.09.017.

[40] Liu Z-Z, Shang X, Dong B, Chai Y-M. Triple Ni-Co-Mo metal sulfides with one-dimensional and hierarchical nanostructures towards highly efficient hydrogen evolution reaction. J Catal 2018;361:204−13. https://doi.org/10.1016/j.jcat.2018.03.004.

[41] Eliaz N, Sridhar TM, Gileadi E. Synthesis and characterization of nickel tungsten alloys by electrodeposition. Electrochim Acta 2005;50:2893−904. https://doi.org/10.1016/j.electacta.2004.11.038.

[42] Lammel P, Rafailovic LD, Kolb M, Pohl K, Whitehead AH, Grundmeier G, Gollas B. Analysis of rain erosion resistance of electroplated nickel−tungsten alloy coatings. Surf Coating Technol 2012;206:2545−51. https://doi.org/10.1016/j.surfcoat.2011.11.009.

[43] Abu-Zied BM, Soliman SA, Asiri AM. Role of rubidium promotion on the nitrous oxide decomposition activity of nanocrystalline Co3O4-CeO2 catalyst. Appl Surf Sci 2019;479:148−57. https://doi.org/10.1016/j.apsusc.2019.01.200.

[44] Kumar A, Jayasankar K, Debata M, Mandal A. Mechanical alloying and properties of immiscible Cu-20 wt.% Mo alloy. J Alloy Compd 2015;647:1040−7. https://doi.org/10.1016/j.jallcom.2015.06.129.

[45] Obalová L, Karásková K, Wach A, Kustrowski P, Mamulová-Kutláková K, Michalik S, Jirátová K. Alkali metals as promoters in Co−Mn−Al mixed oxide for N2O decomposition. Appl Catal Gen 2013;462−463:227−35. https://doi.org/10.1016/j.apcata.2013.05.011.

[46] Chromčáková Ž, Obalová L, Kovanda F, Legut D, Titov A, Ritz M, Fridrichová D, Michalik S, Kuśtrowski P, Jirátová K. Effect of precursor synthesis on catalytic activity of Co3O4 in N2O decomposition. Catal Today 2015;257:18−25. https://doi.org/10.1016/j.cattod.2015.03.030.

[47] Winiarski J, Tylus W, Winiarska K, Szczygieł B. The influence of molybdenum on the corrosion resistance of ternary Zn−Co−Mo alloy coatings deposited from citrate−sulphate bath. Corrosion Sci 2015;91:330−40. https://doi.org/10.1016/j.corsci.2014.11.037.

[48] Sen B, Kuyuldar E, Savk A, Calimli H, Duman S, Sen F. Monodisperse ruthenium-copper alloy nanoparticles decorated on reduced graphene oxide for dehydrogenation of DMAB. Int J Hydrogen Energ 2019;44:10744−51. https://doi.org/10.1016/j.ijhydene.2019.02.176.

[49] Zhu J, Chen C, Li Y, Zhou L, Lan Y. Rapid degradation of aniline by peroxydisulfate activated with copper-nickel binary oxysulfide. Separ Purif Technol 2019;209:1007−15. https://doi.org/10.1016/j.seppur.2018.09.055.

[50] Biesinger MC. Advanced analysis of copper X-ray photoelectron spectra. Surf Interface Anal 2017;49:1325−34. https://doi.org/10.1002/sia.6239.

[51] Li W, Shen X, Zeng R, Chen J, Xiao W, Ding S, et al. Constructing copper-ceria nanosheets with high concentration of interfacial active sites for enhanced performance in CO oxidation. Appl Surf Sci 2019;492:818−25. https://doi.org/10.1016/j.apsusc.2019.06.292.

[52] Sun QQ, Dong YJ, Wang ZL, Yin SW, Zhao C. Synergistic nanotubular copper-doped nickel catalysts for hydrogen evolution reactions. Small 2018;14. https://doi.org/10.1002/smll.201704137.

[53] Laursen AB, Kegnæs S, Dahl S, Chorkendorff I. Molybdenum sulfides—efficient and viable materials for electro - and photoelectrocatalytic hydrogen evolution. Energ Environ Sci 2012;5:5577−91. https://doi.org/10.1039/C2EE02618J.

[54] Sa YJ, Park SO, Jung GY, Shin TJ, Jeong HY, Kwak SK, Joo SH. Heterogeneous Co−N/C electrocatalysts with controlled cobalt site densities for the hydrogen evolution reaction: structure−activity correlations and kinetic insights. ACS Catal 2019;9:83−97. https://doi.org/10.1021/acscatal.8b03446.

[55] Morales-Guio CG, Stern LA, Hu XL. Nanostructured hydrotreating catalysts for electrochemical hydrogen evolution. Chem Soc Rev 2014;43:6555−69. https://doi.org/10.1039/c3cs60468c.

[56] Herraiz-Cardona I, Ortega E, Pérez-Herranz V. Impedance study of hydrogen evolution on Ni/Zn and Ni−Co/Zn stainless steel based electrodeposits. Electrochim Acta 2011;56:1308−15. https://doi.org/10.1016/j.electacta.2010.10.093.

[57] Hitz C, Lasia A. Experimental study and modeling of impedance of the her on porous Ni electrodes. J Electroanal Chem 2001;500:213–22. https://doi.org/10.1016/S0022-0728(00)00317-X.

[58] Herraiz-Cardona I, Ortega E, Perez-Herranz V. Impedance study of hydrogen evolution on Ni/Zn and Ni-Co/Zn stainless steel based electrodeposits. Electrochim Acta 2011;56:1308–15. https://doi.org/10.1016/j.electacta.2010.10.093.

[59] Wu L, Guo X, Xu Y, Xiao Y, Qian J, Xu Y, Guan Z, He Y, Zeng Y. Electrocatalytic activity of porous Ni−Fe−Mo−C−LaNi5 sintered electrodes for hydrogen evolution reaction in alkaline solution. RSC Adv 2017;7:32264–74. https://doi.org/10.1039/C7RA00550D.

[60] Bockris JOM, Potter EC. The mechanism of the cathodic hydrogen evolution reaction. J Electrochem Soc 1952;99:169–86. https://doi.org/10.1149/1.2779692.

[61] Kaninski MPM, Miulovic SM, Tasic GS, Maksic AD, Nikolic VM. A study on the Co-W activated Ni electrodes for the hydrogen production from alkaline water electrolysis - energy saving. Int J Hydrogen Energ 2011;36:5227–35. https://doi.org/10.1016/j.ijhydene.2011.02.046.

[62] Wei M, Yang L, Wang L, Liu T, Liu C, Tang Y, Luo S. In-situ potentiostatic activation to optimize electrodeposited cobalt-phosphide electrocatalyst for highly efficient hydrogen evolution in alkaline media. Chem Phys Lett 2017;681:90–4. https://doi.org/10.1016/j.cplett.2017.05.060.

[63] Peng L, Zheng X, Li L, Zhang L, Yang N, Xiong K, Chen H, Li J, Wei Z. Chimney effect of the interface in metal oxide/metal composite catalysts on the hydrogen evolution reaction. Appl Catal B Environ 2019;245:122–9. https://doi.org/10.1016/j.apcatb.2018.12.035.

[64] Yang L, Zhou H, Qin X, Guo X, Cui G, Asiri AM, Sun X. Cathodic electrochemical activation of Co3O4 nanoarrays: a smart strategy to significantly boost the hydrogen evolution activity. Chem Commun 2018;54:2150–3. https://doi.org/10.1039/C7CC09416G.

[65] Giz MJ, Marengo MC, Ticianelli EA, Gonzalez ER. Electrochemical and physical characterization of Ni-Cu-Fe alloy for chlor-alkali hydrogen cathodes. Eclét Quím 2003;28:21–8.

[66] De Carvalho J, Tremiliosi Filho G, Avaca LA, Gonzalez ER. Electrodeposits of iron and nickel-iron for hydrogen evolution in alkaline solutions. Int J Hydrogen Energ 1989;14:161–5. https://doi.org/10.1016/0360-3199(89)90049-9.

[67] De Giz MJ, Machado SAS, Avaca LA, Gonzalez ER. High area Ni-Zn and Ni-Co-Zn codeposits as hydrogen electrodes in alkaline solutions. J Appl Electrochem 1992;22:973–7. https://doi.org/10.1007/BF01024146.

[68] Chang B, Yang Y, Ye Z, Liu S. Enhancement of alkaline water splitting activity by Co−P coating on a copper oxide nanowire. Dalton Trans 2019;48:891–7. https://doi.org/10.1039/C8DT04419H.

[69] Farinazzo Bergamo Dias Martins P, Papa Lopes P, Ticianelli EA, Stamenkovic VR, Markovic NM, Strmcnik D. Hydrogen evolution reaction on copper: promoting water dissociation by tuning the surface oxophilicity. Electrochem Commun 2019;100:30–3. https://doi.org/10.1016/j.elecom.2019.01.006.